Accepted Manuscript

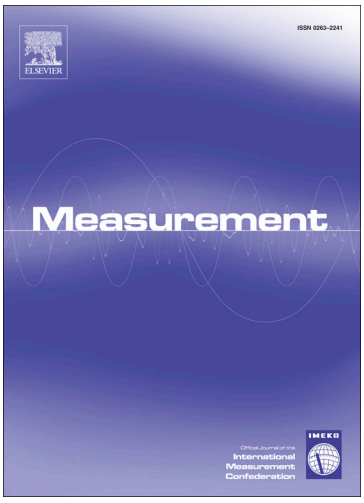

Design and Simulation of a Lithium-ion Battery at Large C-Rates and Varying Boundary Conditions through Heat Flux Distributions

S. Panchal, I. Dincer, M. Agelin-Chaab, R. Fraser, M. Fowler

PII: S0263-2241(17)30747-9
DOI: https://doi.org/10.1016/j.measurement.2017.11.038
Reference: MEASUR 5107

To appear in: *Measurement*

Received Date: 13 April 2016
Revised Date: 25 September 2017
Accepted Date: 13 November 2017

Please cite this article as: S. Panchal, I. Dincer, M. Agelin-Chaab, R. Fraser, M. Fowler, Design and Simulation of a Lithium-ion Battery at Large C-Rates and Varying Boundary Conditions through Heat Flux Distributions, *Measurement* (2017), doi: https://doi.org/10.1016/j.measurement.2017.11.038

Design and Simulation of a Lithium-ion Battery at Large C-Rates and Varying Boundary Conditions through Heat Flux Distributions

S. Panchal[1], I. Dincer[2], M. Agelin-Chaab[2], R. Fraser[1], and M. Fowler[3]

[1] Mechanical and Mechatronic Engineering Department, University of Waterloo, 200 University Avenue West, Waterloo, Ontario, Canada, N2L 3G1

[2] Department of Automotive, Mechanical & Manufacturing Engineering, Faculty of Engineering & Applied Science, University of Ontario Institute of Technology, 2000 Simcoe Street North, Oshawa, Ontario, Canada, L1H 7K4

[3] Chemical Engineering Departments, University of Waterloo, 200 University Avenue West, Waterloo, Ontario, Canada, N2L 3G1

Corresponding Author's Telephone: +1-519-722-4420,

Corresponding Author's Email: satyam.panchal@uwaterloo.ca

Abstract

In this paper, the heat flux distributions on a prismatic lithium-ion battery at 1C, 2C, 3C and 4C discharge rates under various operating temperature or boundary conditions (BCs) of 22°C for air cooling and 5°C, 15°C, and 25°C for water cooling are presented. The goal is to provide quantitative data on the thermal behaviour of lithium-ion batteries. In this regard, a battery thermal management system with water cooling is designed and developed for a 20Ah capacity pouch type lithium-ion battery using dual cold plates. Three heat flux sensors are placed at different locations on the principle surface of the battery: the first near the anode, the second near the cathode, and the third at the mid surface of the body. From these the average and peak heat flux are obtained and presented in this study. In addition to this, the heat flux and voltage distributions are simulated using the neural network approach with the above mentioned discharge rates and BCs. The present results show that increased discharge rates and decreased operating temperature results in increased heat fluxes at the three locations as experimentally measured. Furthermore, the sensors nearest the electrodes (anode and cathode) measured the heat fluxes (and hence temperatures) higher than the sensors located at the center of the battery surface.

Keywords: Lithium-ion battery, thermal management, heat flux, tab temperature, simulation.

1. Introduction

Today, lithium-ion batteries have received much attention in the development of electric vehicles (EVs), hybrid electric vehicles (HEVs), and plug-in hybrid electric vehicles (PHEVs) [1]. Their extensive usage is due to: 1) high specific energy and power densities [2]; 2) high nominal voltage and low self-discharge rate [3]; and 3) long cycle-life and no memory effect [4]. During discharging and charging, precautions

must be taken since, for example exceeding voltage, current or power limits may result in battery cell damage. The possibility of thermal runaways also triggered if care is not properly taken and in addition to this, lithium-ion polymer batteries must be carefully monitored and managed (electrically and thermally) to avoid safety (inflammability) and performance related issues [5, 6].

A lithium-ion battery cells usually has five different layers, namely: the negative current collector, negative electrode (anode), separator, positive electrode (cathode), and positive current collector. The positive electrode materials [7] are typically four types: 1) a metal oxide with layered structure, such as lithium cobalt oxide ($LiCoO_2$ / LCO) [8]; 2) a metal with a three dimensional spinal structure, such as lithium manganese oxide ($LiMn_2O_4$) [9]; 3) lithium nickel manganese cobalt oxide ($LiNiMnCoO_2$/NMC); and 4) a metal with a olivine structure, such as lithium iron phosphate ($LiFePO_4$/LFP) [10]. The anode is usually made of graphite or a metal oxide. The electrolyte can be liquid, polymer or solid. There are several types of lithium-ion batteries available in the market based on their constructions, such as cylindrical, coin, and prismatic. Cylindrical and coin batteries are used in small products such as wristwatches, laser pointers, and slide changers [11], and prismatic batteries are used for high capacity rating such as in automobiles [12].

The safety issues of lithium-ion batteries pose ongoing challenges as the market for lithium-ion technology continues to grow in personal electronics, electric mobility, and stationary energy storage. The severe risks posed by battery thermal runaway necessitate safeguards at every design level – from materials, to cell construction, to module and pack assembly [13]. A battery thermal management system (BTMS) is required in order to secure the desired performance of a battery cell, module or battery pack in a low-temperature environment and the desired lifetime in a high-temperature environment. A typical temperature range for lithium-ion batteries is between 20 and 40°C [14], and an extended range becomes between –10 and +50°C for the tolerable operation [15]. At a high temperature environment, lithium ion batteries degrade rapidly, while in a cold temperature environment, the power output and energy are reduced which ultimately results in reduction of performance and driving range [16]. There are two basic types of cooling systems: i) air cooling, and ii) water cooling. The water cooling is more effective, due to higher specific heat content, as compared to air cooling, and it occupies less volume, but brings more complexities as well as high cost and weight [17].

An understanding of heat generation rate is also important for a thorough understanding of thermal behavior of lithium-ion cell. A number of papers are available for theoretical analysis of heat generation rate as a function of C-rate. There are two main sources for the heat generation in a battery: first, Joule's heating or Ohmic heating and second, the entropy change due to electrochemical reactions [18, 19, 20].

The heat can be endothermic for charging and exothermic for discharge based on the electrode pair. The heat generation rate in a battery is written by:

$$\dot{Q} = I\,(E - V_{act}) - I\left[T\left(\frac{dE}{dT}\right)\right] \quad (1)$$

Here, $I\,(E - V_a)$ is known as the Ohmic or Joule's heating and $I\,[T(dE/dT)]$ is known as the heat generated or consumed due to the reversible entropy change which results from electrochemical reactions within the battery cell. Usually, the second term is small compared to the first term, and therefore negligible for the EV and HEV current rates [21]. In addition to this, heat generation due to side reactions is also generally neglected in theoretical models [22].

There are various mathematical models developed to predict the dynamic behaviors of batteries. An EV designer may use battery models for sizing the required battery and predict the battery performance. The battery models are also used for on-line self-learning performance and SOC estimation in BTMS [23, 24, 25]. There are various papers in the open literature available for battery thermal modeling, using different approaches such as artificial neural network [26, 27], finite element model (FEM) [28] or lumped parameter model (LPM) [29], linear parameter varying (LPV) model [30], or partial differential equation (PDE) model [31]. Christen et al [32] developed a test method for the thermal characterization (in terms of heat capacity and thermal conductivity) using heat flux sensors and temperature of lithium-ion cells and verification of cooling strategies in operation. The heat flux sensor were uniformly arranged around a battery cell with a spatial resolution of 25 mm. They used 69 Ah high energy density lithium mangan oxid prismatic battery cell for testing. Drake et al [22] studied the measurement of heat generation rate in a lithium-ion battery cell at large C-rates (up to 9.6C) through heat flux and temperature measurements. Their method was based on simultaneous determination of heat stored and heat lost from the battery cell through heat flux and temperature measurements and a novel method was established for measurement of the internal temperature of the lithium-ion battery cell. Murashko et al [33] proposed a method for determination of entropy change (ΔS) profile by heat flux measurements of a lithium-ion battery, because the entropy change of a battery has a significant influence on heat generation, especially at lower C-rate currents. Their method also allowed simultaneous measurements of the thermal diffusivity and ΔS for a lithium-ion battery. Wike et al [13] presented an experimental nail penetration study to investigate the effectiveness of phase change composite (PCC) thermal management for preventing propagation when a single battery cell enters thermal runaway on a lithium-ion battery pack. They found that when parallel cells short-circuit through the penetrated battery cell, the packs without PCC propagate fully while those equipped with PCC show no propagation. In all test conditions, the use of PCC lowers the maximum

temperature experienced by neighboring cells by 60 °C or more. Here, for battery modeling, we used neural network approach. Neural networks are usually organized in layers with nodes or neurons connecting different layers through an activation function. Data or pattern is presented at the input layer which travels to the hidden layers through weighted connections and is finally processed at the output layer which represents the output of the network.

Note that experimental tests under varying cooling conditions appear to be more difficult and more expensive. Undertaking both experimental investigation and simulation studies is absolutely very much demanded. The present work in fact does it. In addition, a comprehensive investigation and simulation is conducted on the lithium-ion battery performance under different constant current discharge rates of 1C, 2C, 3C and 4C and boundary conditions (BCs) of 5°C, 15°C and 25°C for water cooling and 22°C for air cooling, and the performance is evaluated in this regard. Furthermore, we designed and developed an experimental facility which is capable of testing different types of batteries with different kind of chemistries. To the best of the authors' knowledge no similar studies on prismatic lithium-ion battery have been reported in the open literature.

2. Experimental Study

In this section, the experimental details are provided through the experimental set-up, battery and cold plate set-up, heat flux sensors locations, thermal data acquisition system, battery cooling system, experimental plan and procedure, and experimental uncertainty.

2.1 Experimental Set-up

The experimental set-up used for this work is shown in Figure 1. A hybrid test bench was originally designed and built to test various hybrid technologies and assess their usefulness in vehicle design. However, the hybrid test bench has been modified to test batteries on different duty cycles and to measure battery thermal performance and degradation. There were two data acquisition (DAQ) used in the tests to log the battery data. The one used to log the battery electrical data such as tine, charge current, discharge current, charge voltage, and discharge voltage, and the second used for thermal data such as heat flux and temperature. Both the electrical and thermal data were recorded every 1 second. Computer-1 provides the basic controls using LabVIEW VI to the controller and load box via RS-232 cables, and the power supply with an Ethernet cable. The computer also offers a GUI for the user to monitor the progress of the experiment. The controller uses analog I/O signal wiring to communicate with the relays and measure the battery voltage. The controller transmits the measured battery voltage back to computer-1. Computer-1 sets the current or voltage values on the load box and power supply, depending on the experiment. The

current, measured internally of the load box and power supply, is transmitted back to computer-1. Depending on the computer requests, the power supply or load box will provide power to or draw power from the battery, respectively. Computer-2 provides the thermal data via the Keithley data acquisition system.

The battery and cold plate set-up is shown in Figure 2 (a). Two commercial available cold plates were used for this experimental work in order to remove the heat generated from the lithium-ion battery during discharge. A 20Ah lithium-ion prismatic battery was used for this experimental work and Table 1 tabulates the cell specifications. There were three thin-film heat flux sensors (HFS) installed on the principal surface of the battery. The locations of these three sensors are shown in Figure 2 (b), and the x and y coordinates of the HFS center points presented in Figure 2 (b) are given in Table 2. These sensors function as a self-generating thermopile transducer. They require no special wiring, reference junctions or signal conditioning. The HFS utilizes a multi-junction thermopile construction on a polyimide film laminate. The output of the sensors provides an average measurement of surface heat flux in a 25.4 x 25.4 mm area (1 $inch^2$). Kapton-backed adhesive tape is used to attach the heat flux sensors to the surface of the battery. In addition to HFS, three thermocouples (TC) were pasted, one near the cathode, another near the anode, and the third one near the mid body. Finally, two more thermocouples were used to measure the tab (electrode or current collector) temperatures during different discharge rates at various boundary conditions.

All measurements were performed using a Keithley 2700 data acquisition system. A 20 channel M7700 analog input module was used to connect to the output terminals of all the instruments. Data logging was programmed and controlled by a Windows based Excel add-in patch, “ExcelLink” that provides instantaneous recording of values on an Excel sheet. This software is particularly useful as the immediate Excel format is easy to work with. Sensors monitored by the thermal data collection system consisted of the following types: thermocouples (TC) and HFS. The majority of sensors were placed on the battery surfaces within the compression rig, while the remaining sensors were installed on the battery cooling system. The battery cooling system consisted of a closed loop of tubing, connecting two cooling plates (P1, P2) to a Fisher Scientific Isotemp 3016 fluid bath. Sensors were placed along the flow path to record properties of the fluid. A schematic diagram of the system is shown in Figure 3 (a), and its picture is shown in Figure 3 (b). The cooling plates (one on top surface and the other on the bottom surface of the battery) were placed within the compression rig directly against the principal surfaces of the battery, such that heat generated within the battery was principally removed by conduction to the surfaces of the cooling plates.

2.2 Experimental Procedure

In the experimental measurements, three different operating temperatures or coolant temperatures or boundary conditions were used for water cooling method: 5°C, 15°C, and 25°C and for air cooling method: 22°C, Four different discharge rates (constant current) were selected: 1C, 2C, 3C, and 4C. The charge rate (constant current-constant voltage) is 1C. The experimental plan is shown in Table 3. The following procedure was performed: i) the isothermal fluid bath and pump was turned on, at least, two hours prior to beginning the cycling in order to bring the battery, bath and compression rig to a steady state temperature. The valves leading to the cold plates were observed and set to open. The isothermal fluid bath was set to the desired cooling temperature or BCs of 5 °C, 15 °C, and 25 °C for the test. ii) The LabVIEW code for the charge/discharge stand (battery electrical data collection) was loaded and relevant test parameters, such as charge current discharge current, charge voltage, discharge voltage, and sampling rate were input to the program. iii) The thermal data acquisition PC (Computer-2) and Keithly 2700 were turned on and allowed to initialize. On the PC, the Excel Link recording software was prepared for data acquisition such as heat flux and water inlet and outlet temperature at the top and bottom of the cold plate. From the measured experimental data, the internal resistance (r_{int}) can also be calculated based on the Ohm's law (covering the voltage drop is divided by current values) as follows:

$$r_{int} = \frac{\Delta V}{I} = \frac{V_{oc} - V_{act}}{I} \tag{2}$$

2.3 Experimental Uncertainty Analysis

In this section, the uncertainty analysis of the experimental measurements and derived correlations are presented. The accuracy of the measurement equipment is determined and used to establish the uncertainty of calculated relationships and properties. The overall uncertainty of the experimental results and theoretical predictions will be calculated using the method described by Moffat in [34]. Evaluating the uncertainty of surface heat flux measurements and the area measurements was required to determine the overall uncertainty of the average surface heat flux measurement. In this method, the result S of an experiment is determined from a set of measurements M as follows:

$$\mathrm{S} = \mathrm{S}\left(\mathrm{M}_1, \mathrm{M}_2, \mathrm{M}_3, \ldots, \mathrm{M}_\mathrm{N}\right) \tag{3}$$

Each measurement can be represented as $M_\mathrm{i} \pm \delta M_\mathrm{I}$ where δM_I is the uncertainty. The effect of each measurement error on the calculated result is determined as

$$\Delta S_{M_i} = \frac{\delta S}{\delta M_i}\delta M_i \tag{4}$$

Hence, the overall uncertainty of the result is determined using Equation (5):

$$\delta S = \left\{\sum_{i=1}^{N}\left(\frac{\delta S}{\delta M_i}\delta M_i\right)^2\right\}^{1/2} \tag{5}$$

If S is described by an equation of the form $S = M_1^a\, M_2^b\, M_3^c \cdots\cdots M_N^m$, then the overall uncertainty of the result can be determined directly from the set of individual measurement uncertainties as described in Equation (6).

$$\frac{\delta S}{S} = \left\{\left(a\frac{\delta M_1}{M_1}\right)^2 + \left(b\frac{\delta M_2}{M_1}\right)^2 + \cdots + \left(m\frac{\delta M_N}{M_1}\right)^2\right\}^{1/2} \tag{6}$$

The heat flux at locations was determined from the product of voltage readings made with the Keithley hardware and the reported sensitivity of the sensor (HFS). The uncertainty in the HFS voltage readings based on the Keithley specifications in the range of 100 mV is given by Equation (7):

$$\frac{\delta V_{HFS}}{V_{HFS}} = \pm\left(3.0 \times 10^{-5} + \frac{3.5 \times 10^{-6}}{V_{HFS}\,[V]}\right) \tag{7}$$

A summary of the uncertainty for heat flux, and the flow rate of water to the upper and bottom cold plates is given in Table 6.

3. Model Development

Using the neural network approach, the battery thermal model is developed for heat flux and voltage simulations based upon the data acquired (time, voltage, current, temperature, heat flux, and charge/discharge rate) from the thermal boundary condition test apparatus using dual cold plates for a 20Ah lithium-ion battery. The neural network architecture for the battery model is shown in Figure 4. There were total 8394 samples considered for this model, and out of 8394 samples, 70% samples (5875) were used for training the model. Also, 15% samples (1259) were used for validation and finally 15% samples (1259) were used for testing the model. There are three inputs to the model while the selected numbers of hidden neurons are six. These three inputs mentioned in below sub sections (3.1.1, 3.1.2, and 3.1.3) are specifically selected because these inputs have a great impacts on the entire performance of the battery during discharging. The number of hidden neurons is six because the regression value is close to one at these neurons. There are three methods for training the algorithm: 1) Levenberg-Marquardt

Method, 2) Bayesian Regularization Method and, 3) Scaled Conjugate Gradient Method. For training the model, method 1) the Levenberg-Marquardt Method was used as the default training algorithm for the feed-forward network in many commercial solvers including MATLAB, due to its robust nature. This algorithm takes more memory, but less time. It automatically trains when generalization stops improving, as indicated by an increase in the mean square error (MSE) of the validation samples. The model was trained several times until the MSE is minimum and regression value (R) is close to one, which implied that there is a close relationship between the targets and outputs.

3.1 Input Training Data

There are basically three inputs to the model. They are discussed in the following subsections.

3.1.1 Boundary Condition or Ambient Temperature

The external temperature (i.e., BCs) has a great effect on the battery performance. Therefore, to increase the accuracy of the modeling, the BCs or ambient temperature have been considered over the same time period and granularity as in the output.

3.1.2 Charge and Discharge Current

This is basically the charge and discharge rate for the battery that is being discharged at a constant current. This rate basically increases the battery surface temperatures as discharge progresses. The charge rate is 1C while the discharge rates are 1C, 2C, 3C and 4C. The discharge current is taken as positive and the charge current is taken as negative.

3.1.3 Battery Capacity

The battery discharge capacity is measured over the entire time period. This is typically measured with the discharge current multiplied by the time in hours over the entire discharge of the battery for the above mentioned discharge rates. The capacity is the time integral of the current and is calculated by using Equation (8).

$$Capacity = Ah = \int_0^t (i)\, dt \tag{8}$$

3.2 Output Training Data

In the output file, there is one output for heat flux. The heat flux (target) of the battery is simulated based on the target. The data is measured with a sampling period of 1 second over a time horizon of 24 hours.

The regression plot is shown in Figure 5. It plots the regression relation between the actual output and the targets. A histogram showing the difference between the actual and the target output is also plotted and among the total samples considered, the majority of errors lie in the range of -0.86 to 0.88.

4. Benchmark Results

After the controlled experimental and model development study described in the preceding, this section explains the results obtained for a particular prismatic lithium-ion battery at different discharge rates (1C, 2C, 3C and 4C) for air cooling (BCs of 22°C) as well as water cooling (BCs of 5°C, 15°C, and 25°C) method.

4.1 Heat Flux, Surface Temperature, and Tab (Electrode) Temperature Profile

Figure 6 (a) shows the heat flux profiles at 4C discharge rate for air cooling method (an ambient 22 °C BC). Note that HFS 1 is located near the positive electrode or cathode, HFS 2 is located near the negative electrode or anode, and HFS 3 is located at the middle of the cell (mid body) along the height of the cell as shown in Figure 2 (b). For the particular case of 4C discharge and 22 °C BC of air cooling, the peak heat flux values are 586.72 W/m^2 near the cathode, 667.88 W/m^2 near the anode, and 303.09 W/m^2 near the mid body. Similarly, the average heat flux values for the above mentioned case are 301.84 W/m^2 near the cathode, 340.07 W/m^2 near the anode, and 147.60 W/m^2 near the mid body. Hence, it is observed that the values are higher near electrodes (cathode and anode) as compared to the mid body. Similar results of average and peak heat flux for an air cooling method are obtained for 2C, 3C, and 4C discharge rate and are tabulated in Table 4 and Table 5.

Figure 6 (b) shows the surface temperature near the cathode, the anode, and the mid body. Just to refresh the reader, three thermocouples (TC) were pasted near electrodes, the first near the cathode, the second near the anode, and the third near the mid body. In general it is observed from the figure that the surface temperature increases as discharge progresses. For this particular case of 4C discharge rate and BC of ambient 22 °C (air cooling) the maximum surface temperature at the end of discharge is 44.21 °C near the cathode, 44.70 °C near the anode, and 40.70 °C near the mid body. Similarly, for the lower C-rates of 1C discharge, the maximum surface temperature at the end of discharge is 29.84 °C near the cathode, 30.1 °C near the anode, and 29.27 °C near the mid body.

Figure 6 (b) also shows the tab temperature for the positive and the negative current collector. Please note that, two more thermocouples were used to measure the tab (electrode or current collector) temperature values during different discharge rates at various boundary conditions. It was found that the tab temperature is always higher for all C-rates and for this particular case of 4C discharge rate and BC of ambient 22 °C (air cooling) the maximum tab temperature at the end of the discharge rate is 54.75°C for positive current collector and 53.62°C for the negative current collector. Also, for the 1C discharge and 22°C BC, the maximum tab temperature at the end of the discharge rate is 30.21°C for positive current collector and 29.27°C for the negative current collector. The positive current collector temperature is

always higher than the negative current collector for all the discharge rates and this is obvious result as the joule heating is the dominating effect and the current flows from positive current collector to the negative current collector during discharging. Finally, it was observed that the temperature distributions are always higher near electrodes as compared to the mid body.

4.2 Average Heat Flux Profile

Figure 8 (a), Figure 9 (a), and Figure 10 (a) show a comparison of the heat fluxes measured by the three heat flux sensors obtained at different discharge rates of 1C, 2C, 3C and 4C and various BCs of 5°C, 15°C, and 25°C for water cooling together with the values predicted by the neural network model. Here, the strong agreement between the experimental and simulation data demonstrates the robustness and accuracy of the model. In contrast to Figure 8 (a), Figure 9 (a) shows the average of all three heat flux sensors under cooling scheme 2 (or BC); that is the inlet cooling water temperature was taken to be 15°C. From the results in Figure 9 (a), it can be seen that the heat flux values are higher under higher cycling rates. This is an expected result when the joule heating dominates the heat generation process. Similarly, the effect of BCs of 25°C on the heat flux distributions can be seen in Figure 10 (a). As a common result, it is found that as the C rate increases, the heat flux begins to rise significantly. It is also observed that the highest average heat fluxes were measured at HFS 1 and HFS 2 for 4C discharge rates and 25°C cooling. In general, for all tests, the sensors nearest the electrodes (HFS 1 and 2) measured heat fluxes higher than the sensor located at the middle of the battery surface. The trend observed is that increased discharge rates (between 1C, 2C, 3C, and 4C) and decreased operating temperature (between 25 °C, 15 °C, and 5 °C), results in increased average heat fluxes at the three locations measured.

The values of average heat fluxes as shown in Figure 8 (a), Figure 9 (a), and Figure 10 (a) under different water cooling conditions (controlled BCs) are tabulated and presented in Table 4. For the air cooling cases, the average heat flux of HFS 2, near the positive electrode is always highest. Liquid cooling cases do not show a definitive pattern between HFS 1 and 2. This is likely due to the slightly uneven cooling gradient across the cold plate. The coolant temperature and thus plate heat flux increases across the width of the battery surface as heat is absorbed. This is in contrast to the air cooling case, where the vertical orientation of the battery provided a condition where cooling potential is approximately equal across the width of the surface. It could be inferred that the air cooling cases are a better representation of the differences in heat generation between the three locations.

4.3 Peak Heat Flux Profile

In Table 5, the peak heat fluxes measured by the three heat flux sensors for all operating temperatures (5 °C, 15 °C, and 25 °C) for water cooling and air cooling (22 °C) are given against discharge rates of 1C,

2C, 3C, and 4C. It is observed that the highest peak heat fluxes were always measured at HFS 2 (near anode). In general, for all tests the sensors nearest the cathode and anode (HFS 1 and 2) measured greater peak heat fluxes than the sensor located at the middle of the battery surface because the heat generation is higher near electrodes than any other locations on the surface of the battery. The trend observed is that increased discharge rates results in increased peak heat fluxes at the three locations measured. For water cooling method, the peak heat flux (3898.71 W/m^2) is highest for the 4C discharge rate and 15 °C BC near the anode and the lowest for (194.56 W/m^2) for the 4C discharge rate and 25 °C BC near the mid body.

4.4 Discharge Voltage Profile

Figure 8 (b), Figure 9 (b), and Figure 10 (b) show a comparison of the measured discharge terminal voltage obtained at different C rates and varying BCs (5 °C, 15 °C, and 25 °C for water cooling) with the values predicted by the neural network model. Overall, it shows a good agreement between the experimental and simulation data, which is indicative of the accuracy of the present model. The model is validated by constant current discharge experiments at current rates ranging from 1C (20A) to 4C (80A), at operating temperatures or BCs ranging from of 5°C to 25°C. Here, the cell is charged with constant current-constant voltage (CC-CV) protocol until the voltage reaches 3.7V and discharged with the constant current (CC) until the voltage drops to 2.0V. A model-experimental comparison for 5°C is shown in Figure 8 (b) for the full cell, where it is seen that the predictions match the experimental data quite well for a wide range of C-rates. At lower discharge rates, the cell potential stays close to the cell's open circuit potential (OCP). As the C rates increase, the cell voltage deviates significantly from the OCP due to the ohmic, activation and mass transport losses. In contrast to Figure 8 (b), Figure 9 (b) shows the voltage validation under cooling scheme 2 (or BC); that is the inlet cooling water temperature was taken to be 15°C. It is observed that the discharge capacity decreases with a decrease in the boundary conditions. The trend observed is that increased discharge rates (between 1C, 2C, 3C, and 4C) and decreased operating temperature (between 25 °C, 15 °C, and 5 °C) results in decreased discharge capacity. For air cooling (BC of 25 °C) method, the discharge voltage profiles at different C-rates can be seen in Figure 8 (b), where the discharge capacity is around 18.5 Ah for all C-rates and it stays closer to the manufacturer's provided data sheet (20 Ah).

5. Conclusions

This paper has presented a comparative study of the heat flux distributions on a prismatic lithium-ion battery cell using both experimental and simulation methods for both air cooling and water cooling techniques. In the experimental study, the dual cold plates approach with the indirect liquid cooling

method (or water cooling) was used. The heat flux distributions on a lithium-ion battery at 1C, 2C, 3C and 4C discharge rates and different BCs of 5°C, 15°C, and 25°C (and also 22°C for air cooling) were studied. The average and peak heat flux values are also obtained from the experimental data analysis. Computationally, a high-fidelity neural network model was developed, and the simulated data were then validated using the experimental data for heat flux and voltage profiles. The developed model successfully captured the charge/discharge behaviour over a wide range of C-rates and BCs. The influences of the cold plates on the battery surface heat flux were also studied. Some concluding remarks are as follows: (i) The heat flux distributions increase as the C-rates increase for both air cooling and water cooling. (ii) For water cooling, increasing discharge rates (between 1C and 4C) and decreasing operating temperature (between 25 °C and 5°C) increase the heat fluxes measured at three locations. (iii) The heat flux sensors closest to the anode and cathode provide higher heat fluxes than the centerline-heat flux sensors located at the middle of the battery surface for both air cooling and water cooling. (iv) The heat fluxes and surface temperatures values are lower for air cooling as compared to the water cooling. (v) The tab (electrode or current collector) temperatures are always higher as compared to the surface temperatures and also the positive current collector temperature is always higher than the negative current collector for all the discharge rates. These results are expected to provide insights into the design and optimization of battery systems. Future work will focus on more rigorous thermal testing under controlled BCs of -5°C, -15°C, and -25°C. Another problem that will be investigated in future is the effect of the discharge rate on the performance of the battery at higher discharge rates of 5C and 6C.

Nomenclature

^{o}C	=	degree Celsius
cm	=	distance in centimeters
mm	=	distance in millimeter
I	=	current [A]
mL	=	milliliter
mV	=	millivolt
min	=	minute
$\dot{Q}$		Heat generation rate [W]
δ	=	delta
q	=	heat flux [W/m^2]
T	=	temperature [°C or K]
t	=	time [s]

V = cell voltage or cell potential [V]

dE/dT = Temperature coefficient [V/°C]

Subscripts

act = actual

chg = charge

dis = discharge

int = internal

sim = simulated

x,y,z = Cartesian coordinate directions

Acronyms

A	Ampere
Ah	Ampere-hour
BC	Boundary condition
BTMS	Battery thermal management system
C	Capacity
CC	Constant-current
CV	Constant-voltage
DAQ	Data acquisition
EV	Electric vehicle
HF	Heat flux
HFS	Heat flux sensor
HEV	Hybrid electric vehicle
GUI	Graphical user interface
I/O	Input/output
LabVIEW	Laboratory virtual instrument engineering workbench
$LiCoO_2$	Lithium cobalt oxide
$LiMn_2O_4$	Lithium manganese oxide
$LiNiMnCoO_2$	Lithium manganese cobalt oxide
$LiFePO_4$	Lithium iron phosphate
LCO	Lithium cobalt oxide
LFP	Lithium phosphate
LPM	Lumped parameter model
LPV	Linear parameter varying

MSE	Mean square error
NMC	Lithium manganese cobalt oxide
OCP	Open circuit potential
PHEV	Plug-In hybrid electric vehicle
PDE	Partial differential equation
TC	Thermocouple
R	Regression
RS-232	Recommend standard number 232
SOC	State of charge
S	results

References

[1] Q. Wang, Q. Sun, P. Ping, X. Zhao, J. Sun and Z. Lin, "Heat transfer in the dynamic cycling of lithium–titanate batteries," International Journal of Heat and Mass Transfer, no. 93, pp. 896-905, 2016.

[2] Z. Ling, F. Wang, X. Fang, X. Gao and Z. Zhang, "A hybrid thermal management system for lithium ion batteries combining phase change materials with forced-air cooling," Applied Energy, no. 148, pp. 403-409, 2015.

[3] A. Ritchie and W. Howard, "Recent developments and likely advances in lithium-ion batteries," Journal of Power Sources, vol. 162, pp. 809-812, 2006.

[4] Y. Ye, L. H. Saw, Y. Shi and A. A. Tay, "Numerical analyses on optimizing a heat pipe thermal management system for lithium-ion batteries during fast charging," Applied Thermal Engineering, vol. 86, pp. 281-291, 2015.

[5] X. Feng, M. Fang, X. He, M. Ouyang, L. Lu, H. Wang and M. Zhang, "Thermal runaway features of large format prismatic lithium ion battery using extended volume accelerating rate calorimetry," Journal of Power Sources, pp. 255 : 294-301, 2014.

[6] L. Lu, X. Han, J. Hua, M. Ouyang and J. Li, "A review on the key issues for lithium-ion battery management in electric vehicles," Journal of Power Sources, pp. 226:272-288, 2013.

[7] K. Yeow, M. Thelliez, H. Teng and E. Tan, "Thermal Analysis of a Li-ion Battery System with Indirect Liquid Cooling Using Finite Element Analysis Approach," SAE International Journal, vol. 1, no. 1, pp. 65-78, 2012.

[8] L. Y. Shao-Horn, C. Delmas, C. E. Nelson and M. A. O'Keefe, "Atomic resolution of lithium ions in

LiCoO2," Nature Materials, vol. 2, pp. 464-467, 2003.

[9] C. Julien, "Local Structure of lithiated manganese oxides," Solid State Ionics, vol. 177, pp. 11-19, 2006.

[10] J. T. Bloking, S. Y. Chung and Y. M. Chiang, "Electrically conductive phospho-olivines as lithium storage electrodes," Nature Materials, vol. 1, pp. 123-128, 2002.

[11] J. Dahn and G. M. Ehrlich, "Lithium-Ion Batteries," in Linden's Handbook of Batteries, New York, McGraw Hill, 2011, pp. 26.1-26.79.

[12] J. Yi, U. S. Kim, C. B. Shin, T. Han and S. Park, "Three-dimensional thermal modeling of a lithium-ion battery considering the combined effects of the electrical and thermal contact resistances between current collecting tab and lead wire," Journal of the Electrochemical Society, vol. 160, no. 3, pp. 437-443, 2013.

[13] S. Wilke, B. Schweitzer, S. Khateeb and S. Al-Hallaj, "Preventing thermal runaway propagation in lithium ion battery packs using a phase change composite material: An experimental study," Journal of Power Sources, vol. 340, pp. 51-59, 2017.

[14] H. Teng, Y. Ma, K. Yeow and M. Thelliez, "An Analysis of a Lithium-ion Battery System with Indirect Air Cooling and Warm-Up," SAE International Journal of Passenger Cars- Mechanical Systems, vol. 4, no. 3, pp. 1343-1357, 2011.

[15] F. He and L. Ma, "Thermal Management in Hybrid Power Systems Using Cylindrical and Prismatic Battery Cells," Heat Transfer Engineering, vol. 37, no. 6, pp. 581-590, 2016.

[16] B. Wu, V. Yufit, M. Marinescu, G. J. Offer, R. F. Martinez-Botas and N. P. Brandon, "Coupled thermal–electrochemical modelling of uneven heat generation in lithium-ion battery packs," Journal of Power Sources, vol. 243, pp. 544-554, 2013.

[17] G.-H. Kim, A. Pesaran and R. Spotnitz, "A three-dimensional thermal abuse model for lithium-ion cells," Journal of Power Sources, vol. 170, no. 2, pp. 476-489, 2007.

[18] C. R. Pals and J. Newman, "Thermal modeling of the lithium/polymer battery," Journal of the Electrochemical Society, vol. 142, no. 10, pp. 3274-3281, 1995.

[19] Y. Chen and J. W. Evans, "Three-dimensional thermal modeling of lithium-polymer batteries under galvanostatic discharge and dynamic power profile," Journal of the Electrochemical Society, vol. 141, no. 11, pp. 2947-2952, 1994.

[20] G. Wierschem, B. McKinney and E. Nrotek, "Thermal management of lead-acid batteries for electric vehicles," in Research and developement testing, Detroit, 1993.

[21] K. Smith and C.-Y. Wang, "Power and thermal characterization of a lithium-ion battery pack for

hybrid-electric vehicles," Journal of Power Sources, vol. 160, no. 1, pp. 662-673, 2006.

[22] S. J. Drake, M. Martin, D. A. Wetz, J. K. Ostanek, S. P. Miller and A. Jain, "Heat generation rate measurement in a Li-ion cell at large C-rates through temperature and heat flux measurements," Journal of Power Sources, vol. 285, pp. 266-273, 2015.

[23] O. Erdinc, B. Vural and M. Uzunoglu, "A dynamic Lithium-ion Battery Model Considering the Effects of Temperature and Capacity Fading, Clean Electrical Power," in International Conference, IEEE, pp. 383–386., 2009.

[24] L. Lam, P. Bauer and E. Kelder, "A Practical Circuit-Based Model for Li-ion Battery Cells in Electric Vehicle Applications," in In Telecommunications Energy Conference (INTELEC), IEEE 33rd International, pp. 1–9., 2011.

[25] A. Ostadi, M. Kazerani and S. K. Chen, "Optimal Sizing of the Energy Storage System (ESS) in a Battery-Electric Vehicle," Transportation Electrication Conference and Expo (ITEC), IEEE, pp. 1-6, 2013.

[26] S. Panchal, I. Dincer, M. Agelin-Chaab, R. Fraser and M. Fowler, "Experimental and theoretical investigation of temperature distributions in a prismatic lithium-ion battery," International Journal of Thermal Sciences, no. 99, pp. 204-212, 2015.

[27] S. Panchal, I. Dincer, M. Agelin-Chaab, R. Fraser and M. Fowler, "Thermal modeling and validation of temperature distributions in a prismatic lithium-ion battery at different discharge rates and varying boundary conditions," Applied Thermal Engineering, 2015.

[28] A. Pruteanu, B. V. Florean, G. Maria Moraru and R. C. Ciobanu, "Development of a thermal simulation and testing model for a superior lithium-ion-polymer battery," in Optimization of Electrical and Electronic Equipment (OPTIM), IEEE, pages 947–952, 2012.

[29] C. Alaoui, "Solid-State Thermal Management for Lithium-Ion EV Batteries," Vehicular Technology, IEEE Transactions on, vol. 62, no. 1, pp. 98-107, 2013.

[30] X. Hu, S. Asgari, S. Lin, S. Stanton and W. Lian, "A linear parameter-varying model for HEV/EV battery thermal modeling," in Energy Conversion Congress and Exposition (ECCE), IEEE, pages 1643-1649, 2012.

[31] A. Smyshlyaev, M. Krstic, N. Chaturvedi, J. Ahmed and A. Kojic, "PDE model for thermal dynamics of a large," in American Control Conference (ACC), IEEE, pages 959-964, 2011.

[32] R. Christen, G. Rizzo, A. Gadola and M. Stöck, "Test method for thermal characterization of Li-ion cells and verification of cooling concepts," Batteries, vol. 3, pp. 1-12, 2017.

[33] K. Murashko, A. Mityakov, V. Mityakov, S. Sapozhnikov, J. Jokiniemi and J. Pyrhönen, "Determination of the entropy change profile of a cylindrical lithium-ion battery by heat flux

measurements," Journal of Power Sources, vol. 330, pp. 61-69, 2016.

[34] R. J. Moffat, "Uncertainty analysis," in Electronics Cooling-Dedicated to Thermal Management in Electronic Industry, 1999.

List of Table Captions

List of Figure Captions

Tables

Table 1 : $LiFePO_4$- 20Ah lithium-ion pouch cell specifications

Specifications	Value
Cathode Material	$LiFePO_4$
Anode Material	Graphite
Electrolyte	Carbonate based
Nominal Capacity	20.0 Ah
Nominal Voltage	3.3 V
Dimensions	7.25 mm x 160 mm x 227 mm

Table 2 : Locations of heat flux sensor centre-points distance from bottom left corner of the cell surface

Heat Flux Sensor	Location	Type of HFS	X [cm]	Y [cm]
1	Cathode	HFS-1	10.4	16.9
2	Anode	HFS-2	5.2	16.9
3	Mid-body	HFS-3	7.8	12.2

Table 3 : Experimental plan

Cooling Type	Boundary Condition [°C]	Charge Rate	Discharge Rate
Water cooling	5	1C	1C, 2C, 3C, 4C
	15	1C	1C, 2C, 3C, 4C
	25	1C	1C, 2C, 3C, 4C
Air cooling	~22	1C	1C, 2C, 3C, 4C

Table 4 : Summary of average heat flux at 1C, 2C, 3C, 4C discharge rates and different boundary conditions

Cooling Type	Boundary Condition [°C]	Average Heat Flux [W/m^2]				
		Position	1C	2C	3C	4C
Water cooling	5	Cathode	334.23	661.73	976.03	1267.61
		Anode	556.92	1522.257	1766.22	1921.61

Cooling Type	Boundary Condition [°C]	Average Heat Flux [W/m^2]				
		Position	1C	2C	3C	4C
		Mid Body	193.07	504.26	789.70	1061.93
	15	Cathode	454.83	1237.42	1656.41	1882.98
		Anode	359.44	913.17	1667.82	2014.69
		Mid Body	113.68	283.27	512.41	710.18
	25	Cathode	199.63	1226.89	2279.34	1988.01
		Anode	180.42	1170.87	2071.78	2391.31
		Mid Body	71.08	198.19	423.69	605.61
Air cooling	~22	Cathode	41.80	131.30	237.91	301.84
		Anode	47.10	146.73	239.17	340.077
		Mid Body	25.12	72.10	107.37	147.60

Table 5 : Summary of peak heat flux at 1C, 2C, 3C, 4C discharge rates and different boundary conditions

Cooling Type	Boundary Condition [°C]	Peak Heat Flux [W/m^2]				
		Position	1C	2C	3C	4C
Water cooling	5	Cathode	600.69	1053.55	1530.89	2095.22
		Anode	933.20	2289.99	3095.71	3715.23
		Mid Body	508.67	923.68	1314.09	1829.60
	15	Cathode	754.33	1834.25	2753.32	3372.20
		Anode	702.18	1492.86	2928.07	3898.71
		Mid Body	347.98	533.92	920.87	1304.69
	25	Cathode	453.07	1910.05	3276.56	3300.50
		Anode	528.20	1819.36	3106.09	3877.62
		Mid Body	294.56	372.02	883.63	1295.22
Air cooling	~22	Cathode	113.08	268.48	446.56	586.72
		Anode	136.90	258.90	481.68	667.88
		Mid Body	93.58	195.94	233.35	303.09

Table 6 : Summary of uncertainty

Variable	Range	± Relative Uncertainty (%)
$\dot{m}$ [mL/min]	170 mL/min – 218 mL/min	8.3% - 10.6%
ΔT_w [°C]	0.1 °C – 2.6 °C	0 % – 21.9%
q_{HFS} [W/m^2]	0 W/m^2 - 4994 W/m^2	0% - 0.04%

Figures

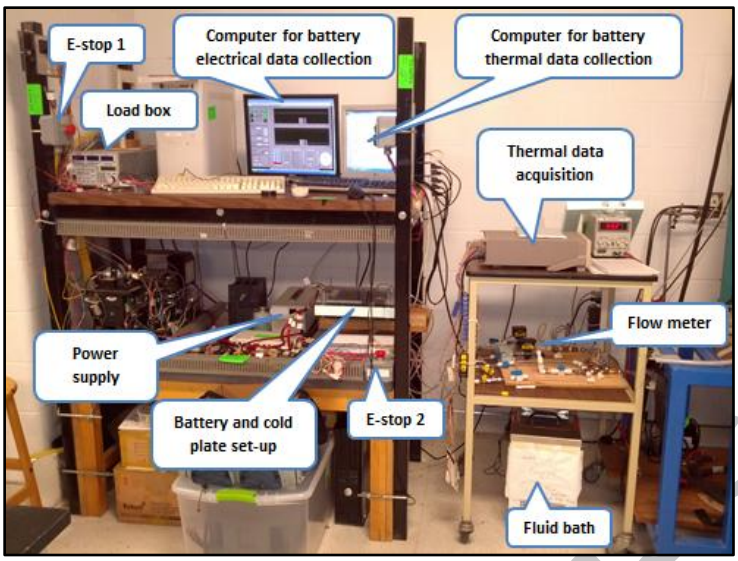

Figure 1 : Experimental set-up

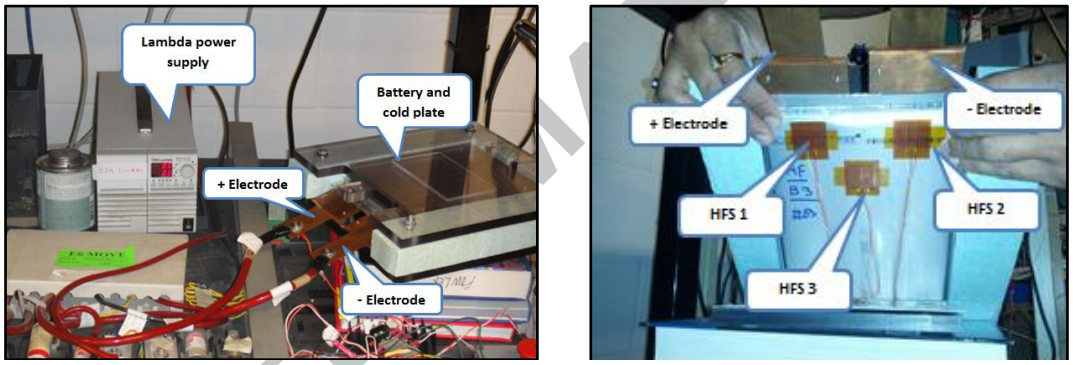

(a) Battery and cold plate set-up **(b) Heat flux sensors locations**

Figure 2 : Battery and cold plate set-up, and heat flux sensors locations

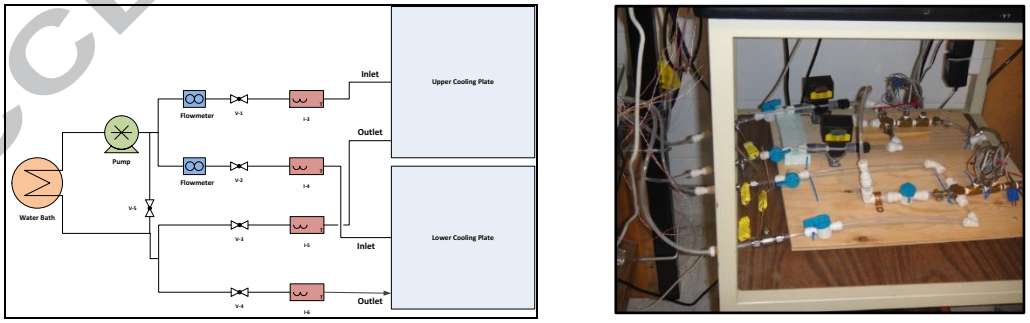

(a) Schematic **(b) Picture**

Figure 3: Cooling system flow from bath to upper and lower cold plates

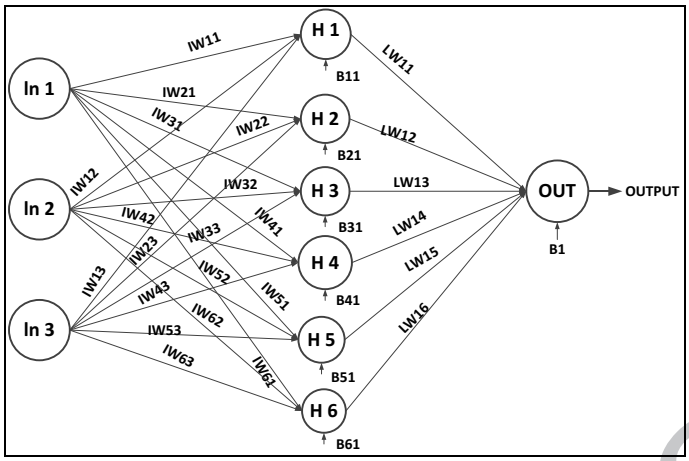

Figure 4 : Neural network architecture

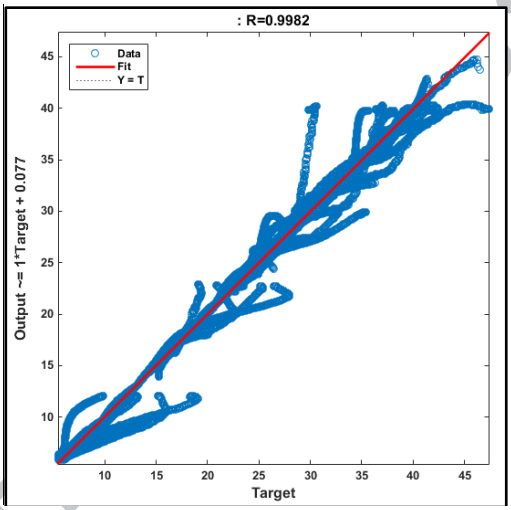

Figure 5 : Regression plot

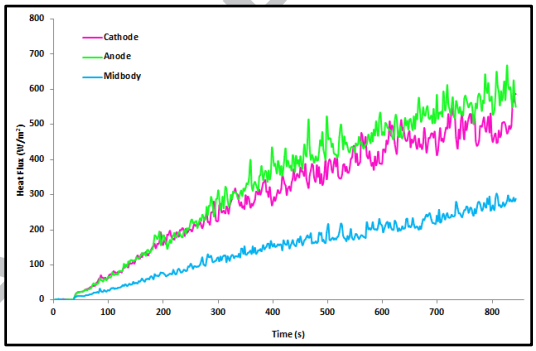

(a) Heat flux profiles at 4C_22 °C ambient

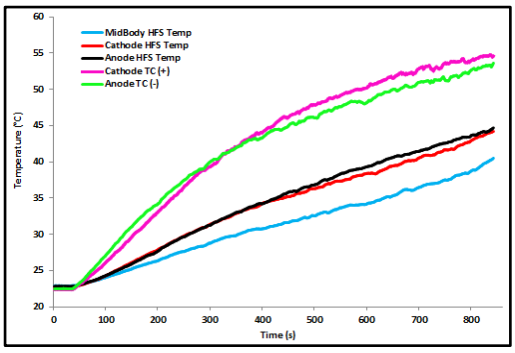

(b) Tab and surface temperature profiles at 4C_ 22 °C ambient

Figure 6 : Heat flux, tab temperature and surface temperature profiles at 4C discharge rate and boundary conditions of 22 °C ambient (air cooling)

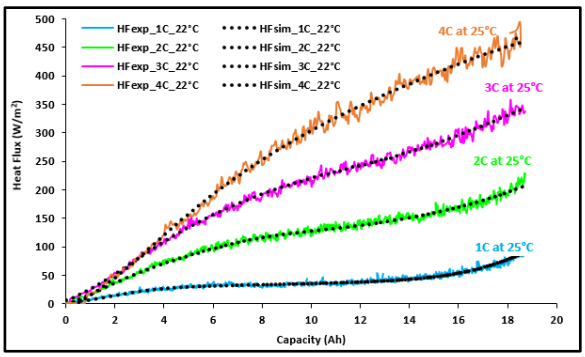

(a) Heat flux profiles at 22 °C ambient

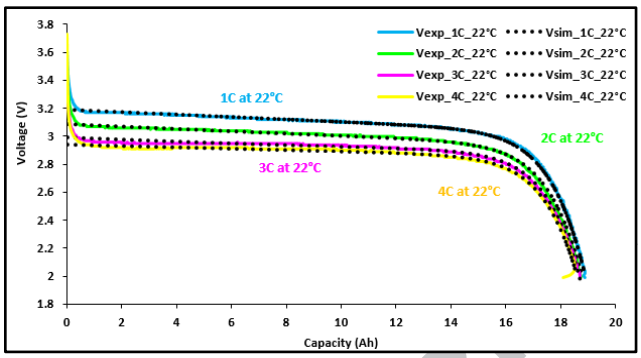

(b) Voltage profiles at 22 °C ambient

Figure 7 : Heat flux and voltage profiles at 1C, 2C, 3C, 4C and boundary conditions of 22 °C ambient (air cooling)

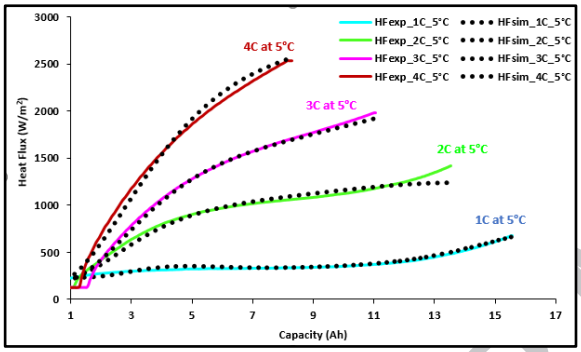

(a) Heat flux profiles at 5 °C

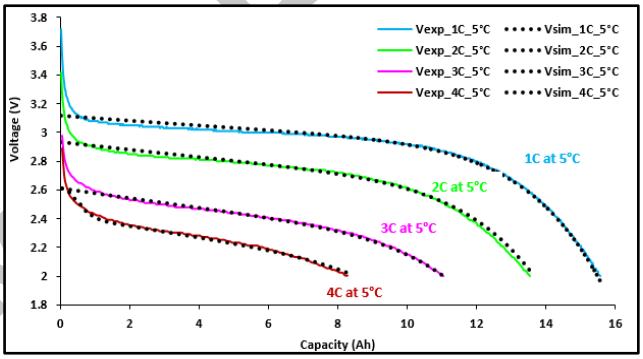

(b) Voltage profiles at 5 °C

Figure 8 : Heat flux and voltage profiles at 1C, 2C, 3C, 4C and boundary conditions of 5 °C(water cooling)

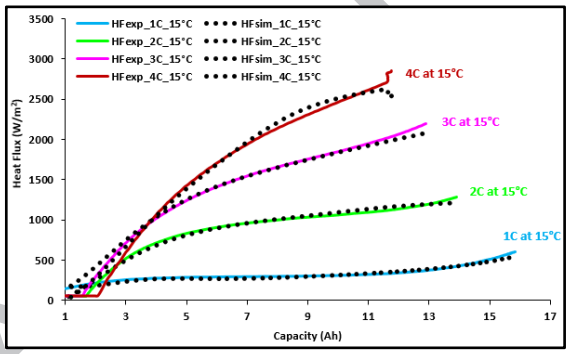

(a) Heat flux profiles at 15 °C

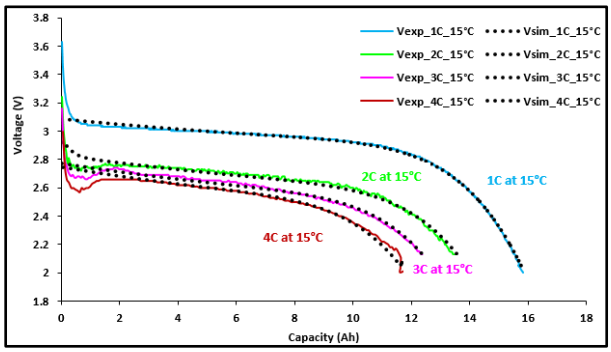

(b) Voltage profiles at 15 °C

Figure 9 : Heat flux and voltage profiles at 1C, 2C, 3C, 4C and boundary conditions of 15 °C(water cooling)

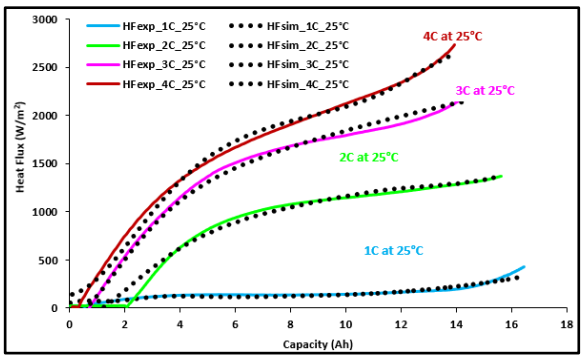

(a) Heat flux profiles at 25 °C

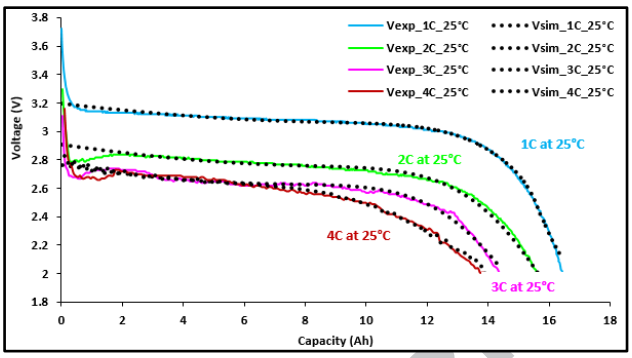

(b) Voltage profiles at 25 °C

Figure 10 : Heat flux and voltage profiles at 1C, 2C, 3C, 4C and boundary conditions of 25 °C(water cooling)

Highlights

- Designed and developed battery cooling system
- Studied average and peak heat flux distributions
- Developed and validated battery thermal model using neural network approach
- Validation of heat flux at different discharge rates and BCs
- Validation of voltage distributions at different discharge rates and BCs